

# Connectivity-Based Parcellation of the Human Orbitofrontal Cortex

Thorsten Kahnt,<sup>1,2,3,4</sup> Luke J. Chang,<sup>5</sup> Soyoung Q Park,<sup>3,6</sup> Jakob Heinze,<sup>1,2</sup> and John-Dylan Haynes<sup>1,2,3</sup>

<sup>1</sup>Bernstein Center for Computational Neuroscience, and <sup>2</sup>Berlin Center for Advanced Neuroimaging, Charité-Universitätsmedizin Berlin, D-10115 Berlin, Germany, <sup>3</sup>Berlin School of Mind and Brain, Humboldt-Universität zu Berlin, D-10117 Berlin, Germany, <sup>4</sup>Laboratory for Social and Neural Systems Research, Department of Economics, University of Zurich, CH-8006 Zürich, Switzerland, <sup>5</sup>Department of Psychology, University of Arizona, Tucson, Arizona 85721, and <sup>6</sup>Department of Education and Psychology, Freie Universität Berlin, D-14195 Berlin, Germany

The primate orbitofrontal cortex (OFC) is involved in reward processing, learning, and decision making. Research in monkeys has shown that this region is densely connected with higher sensory, limbic, and subcortical regions. Moreover, a parcellation of the monkey OFC into two subdivisions has been suggested based on its intrinsic anatomical connections. However, in humans, little is known about any functional subdivisions of the OFC except for a rather coarse medial/lateral distinction. Here, we used resting-state fMRI in combination with unsupervised clustering techniques to investigate whether OFC subdivisions can be revealed based on their functional connectivity profiles with other brain regions. Examination of different cluster solutions provided support for a parcellation into two parts as observed in monkeys, but it also highlighted a much finer hierarchical clustering of the orbital surface. Specifically, we identified (1) a medial, (2) a posterior-central, (3) a central, and (4–6) three lateral clusters spanning the anterior–posterior gradient. Consistent with animal tracing studies, these OFC clusters were connected to other cortical regions such as prefrontal, temporal, and parietal cortices but also subcortical areas in the striatum and the midbrain. These connectivity patterns provide important implications for identifying specific functional roles of OFC subdivisions for reward processing, learning, and decision making. Moreover, this parcellation schema can provide guidance to report results in future studies.

## Introduction

The orbitofrontal cortex (OFC) covers the ventral surface of the primate prefrontal cortex (PFC). It has received considerable attention for its role in processing emotion, reward learning, and decision making (Zald and Rauch, 2008). Subdivisions of the monkey and human OFC have been defined based on its cytoarchitecture (Brodmann, 1909; Walker, 1940; Carmichael and Price, 1994; Ongür et al., 2003; Mackey and Petrides, 2010; Uylings et al., 2010), sulcal topography (Chiavaras and Petrides, 2000), and anatomical connectivity (Carmichael and Price, 1996; Ongür and Price, 2000). In contrast, surprisingly little is known about any functional subdivisions other than a simple medial/lateral distinction (Kringelbach and Rolls, 2004).

The OFC is reciprocally connected to higher sensory areas, medial and lateral PFC, medial temporal lobe structures, the midbrain, and the striatum (for review, see Cavada et al., 2000). In monkeys, two functional OFC subdivisions have been pro-

posed based on its intraregional anatomical connections (Carmichael and Price, 1996; Ongür and Price, 2000): a “medial” network, including the medial and posterior-lateral part of the OFC; and an “orbital” network, covering most of the ventral surface. These two networks exhibit little overlap and are differentially connected to higher sensory cortices (orbital network), the hypothalamus, and the brainstem (medial network) as well as different regions in the striatum. It remains an open question, however, whether similar subdivisions with homogeneous connectivity profiles exist for the human OFC.

During the last decade, monkey electrophysiology as well as noninvasive human functional magnetic resonance imaging (fMRI) have remarkably advanced our knowledge about the functions of the OFC (Kringelbach, 2005; Murray et al., 2007; Wallis, 2007). These studies have provided evidence for a role of the OFC in processing reward value, reward expectancies, and punishments (Tremblay and Schultz, 1999; Gottfried et al., 2003; Padoa-Schioppa and Assad, 2006; Morrison and Salzman, 2009; Kahnt et al., 2010). However, despite its heterogeneous architecture and widespread anatomical connections, only very coarse functional subdivisions of the OFC have been suggested (Kringelbach and Rolls, 2004). Medial OFC has been thought to process rewards, whereas lateral OFC has been suggested to process punishments that signal a need for change in behavior (Elliott et al., 2000; O’Doherty et al., 2001). Moreover, an anterior–posterior gradient reflecting the abstractness of a reinforcer has been suggested as well (Kringelbach and Rolls, 2004). However, it remains unclear whether and how these simplistic func-

Received Jan. 18, 2012; revised March 7, 2012; accepted March 13, 2012.

Author contributions: T.K., L.J.C., S.Q.P., and J.-D.H. designed research; T.K. and J.D. performed research; T.K. analyzed data; T.K., L.J.C., S.Q.P., J.H., and J.-D.H. wrote the paper.

This work was funded by the Bernstein Computational Neuroscience Program of the German Federal Ministry of Education and Research (Grant 01GQ0411), the Swiss National Science Foundation (PP00P1\_128574), and the Excellence Initiative of the German Federal Ministry of Education and Research (Deutsche Forschungsgemeinschaft Grant GSC86/1-2009). We thank Daniel S. Margulies for helpful discussions on previous versions of the manuscript.

Correspondence should be addressed to Thorsten Kahnt, Bernstein Center for Computational Neuroscience, Philippstrasse 13, House 6, D-10115 Berlin, Germany. E-mail: thorsten.kahnt@bccn-berlin.de.

DOI:10.1523/JNEUROSCI.0257-12.2012

Copyright © 2012 the authors 0270-6474/12/326240-11\$15.00/0

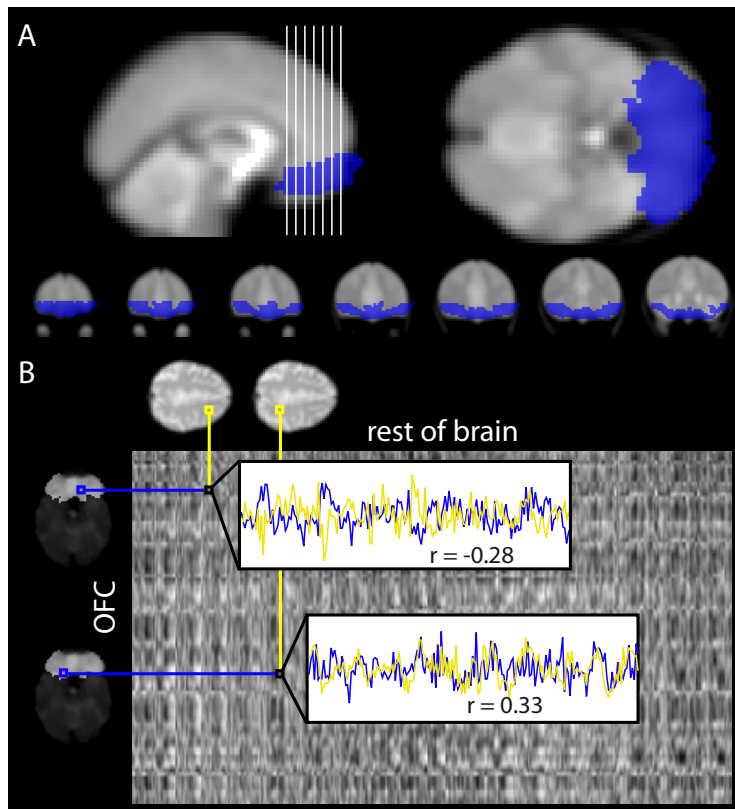


**Figure 1.** OFC region of interest and connectivity patterns. **A**, Voxels in blue are included in a mask of the OFC comprised of standard AAL labels. This mask is overlaid on a mean EPI image (averaged across time and subjects). Coronal sections on the bottom correspond to white vertical lines on the top left. **B**, Sketch of an individual OFC-by-rest-of-brain connectivity matrix. Each cell in the matrix corresponds to the correlation between the resting-state activity in an OFC voxel (blue) and a voxel in the rest of the brain (yellow). Each row represents the connectivity profile of one OFC voxel.

tional OFC divisions are related to the organization of its functional connections.

Here we used resting-state fMRI in combination with unsupervised clustering techniques (Cohen et al., 2008; Kelly et al., 2010; Chang et al., 2012) to parcellate the human OFC exclusively based on its functional connectivity structure with other brain regions. First, we describe different sets of connectivity-based OFC subdivisions. Second, we provide a picture of how these subdivisions are functionally connected with other cortical and subcortical structures. Finally, based on these patterns of confluences, we tentatively propose functional roles for the different OFC subdivisions that can provide a reference frame for reporting and interpreting future neuroimaging results.

## Materials and Methods

**Participants.** Thirteen right-handed subjects [7 female, age (mean  $\pm$  SEM),  $26.31 \pm 1.27$  years] participated in a resting-state scanning session. Subjects received no visual stimulation and were asked to rest but to stay awake during the 6 min of scanning. Before this session, all subjects had participated in a  $\sim 1$  h experimental task (Kahnt et al., 2011a) and were thus familiarized with the MRI environment. Subjects gave written informed consent to participate, and the study was approved by the local ethics review board of the Charité-Universitätsmedizin Berlin.

**fMRI acquisition.** Functional imaging was conducted on a 3 tesla Siemens Trio scanner equipped with a 12-channel head coil. For each subject, 180 T2\*-weighted echo-planar images (EPI) containing 33 slices (3 mm thick) separated by a gap of 0.75 mm were acquired. Imaging parameters were as follows: TR, 2000 ms; TE, 30 ms; flip angle, 90°; matrix size,  $64 \times 64$ ; and FOV, 192 mm; resulting in a voxel size of  $3 \times 3 \times 3.75$  mm. Slices were tilted 30° from the anterior commissure–posterior com-

missure plane for optimal signal coverage in the OFC (Weiskopf et al., 2006). This procedure provided good signal coverage in the OFC (Fig. 1A).

**Preprocessing of fMRI images.** Preprocessing and second-level group statistics were performed using SPM2 (Wellcome Department of Imaging Neuroscience, Institute of Neurology, London, UK). Preprocessing included slice time correction (first slice as reference slice), realignment (to the first volume) and spatial normalization (affine normalization followed by 16 nonlinear iterations with  $7 \times 9 \times 7$  basis functions) to the standard EPI template of the Montreal Neurological Institute (MNI), provided by SPM2. Spatial normalization parameters were used to write two sets of normalized images: one with a voxel size of  $4 \times 4 \times 4$  mm (4 mm set) and one with a voxel size of  $3 \times 3 \times 3$  mm (3 mm set). Both sets were spatially smoothed with a Gaussian kernel of 6 mm FWHM.

**Filtering of fMRI time series.** To denoise the fMRI time series, for each subject the time series of all voxels were filtered (Fox et al., 2009; Van Dijk et al., 2010) using a general linear model (GLM) with the following set of regressors: 1–6, six regressors related to between-scan head movements that were estimated during the realignment procedure; 7, a linear trend; 8, a constant term; 9 and 10, the average white-matter signal from two 7 mm spheres in the left and right frontal white matter ( $[x, y, z] = \pm 22, 38, 6$ ); 11 and 12, the average CSF signal from two 2 mm spheres in the left and right lateral ventricle ( $\pm 15, -27, 23$ ); and 13, the averaged signal from a whole-brain mask. The whole-brain mask included all voxels that are labeled in the standard Automated Anatomical Labeling (AAL) map as well as a box ( $x = -31$  to  $31, y = -32$  to  $9, z = -25$  to  $-3$ ) covering the midbrain. The time series in each voxel was predicted using this set of 13 regressors, and the resulting residuals were high-pass filtered (cutoff = 128 s) and used for all subsequent analyses (Chang et al., 2012). We did not perform low-pass filtering to remove high-frequency signals in the time series. Most high-frequency fluctuations attributable to physiological noise would have been removed by regressing out the global mean and the signal from the CSF and white matter seeds. However, a clustering based on bandpass-filtered data (high-pass: 100.0 s; low-pass: Gaussian filter with half-width at half-maximum = 2.8 s) provided very similar results.

**Definition of region of interest.** We selected the OFC region of interest (ROI) using the following AAL map labels: left and right superior orbital gyrus (5, 6); left and right middle orbital gyrus (9, 10); left and right inferior orbital gyrus (15, 16); left and right medial orbital gyrus (MOG) (25, 26); and left and right rectal gyrus (GR) (27, 28). The resulting ROI included voxels in the left and right medial and lateral orbitofrontal cortex (Fig. 1A). All other AAL labeled voxels (i.e., most gray matter voxels except for the OFC) as well as the box covering the midbrain (see above) were defined as the rest of the brain.

**Connectivity-based parcellation.** Our aim was to parcellate the entire OFC into distinct anatomical subdivisions based on their resting-state connectivity profiles with the rest of the brain. Similar methods have been used to subdivide brain structures using different measures of connectivity such as diffusion tractography (Johansen-Berg et al., 2004; Tomassini et al., 2007; Beckmann et al., 2009), resting-state fMRI (Cohen et al., 2008; Kelly et al., 2010; Kim et al., 2010; Nelson et al., 2010; Cauda et al., 2011), and coactivations (Wager et al., 2009; Eickhoff et al., 2011). In our approach, correlations between the individual filtered fMRI time

series in each OFC voxel and each voxel in the rest of the brain were computed, resulting in a functional connectivity matrix (OFC by “rest of the brain”) for each subject, as detailed below. Second, these individual correlation matrices were averaged across subjects to receive the average connectivity patterns, as detailed below.

More specifically, for each subject, we first computed the Pearson correlation coefficient between the time series in each OFC voxel (from the 3 mm set) and the time series in every other voxel in the brain excluding all OFC voxels (from the 4 mm set; different voxel sizes were used to have sufficiently high spatial resolution in the OFC in conjunction with reasonable computational and memory requirements). This resulted in a 2-D matrix (3141 OFC voxels by 22,192 other voxels in the entire brain) of correlation coefficients where each row reflects the connectivity pattern of one OFC voxel with the rest of the brain (Fig. 1B). Importantly, because voxels are in MNI space, a given voxel has approximately the same anatomical position in all subjects. Thus, individual correlation matrices can be averaged across subjects. To achieve this, the individual correlation matrices were Fisher’s  $Z$ -statistic transformed, averaged across subjects, and back-transformed into Pearson correlation coefficients. The resulting matrix contains the average connectivity pattern for each OFC voxel and provides the basis for the subsequent parcellation method.

Parcellation was performed using a standard  $K$ -means clustering algorithm ( $K$ -means as implemented in the MATLAB Statistics Toolbox, Version 6.1, using the “correlation” option—i.e.,  $1 -$  the correlation between the connectivity patterns of OFC voxels as the distance measure). This algorithm in combination with this distance measure allowed us to compute parcellations with  $K = 2, 3 \dots 10$  clusters of voxels that have a similar pattern of connectivity with the rest of the brain. Thus, voxels are more likely to be clustered together the greater their similarity in connectivity profiles with the rest of the brain. The parcellation was performed for all voxels in both hemispheres simultaneously; that is, for each  $K$ , the connectivity patterns from all OFC voxels were subjected to a single parcellation, regardless of the anatomical position (i.e., hemisphere) of a given voxel. For each  $K$ , we used the best solution from 100 repetitions with different initial centroids. Importantly, this method is entirely data driven, unsupervised, and works without any anatomical constraints. To rule out the possibility that the observed clusterings are strongly influenced by the specific distance measure that was used, we also computed the parcellations using squared Euclidean distance. The resulting clusterings were very similar to the clusterings obtained by using correlation as distance measure.

**Between-subject stability of connectivity patterns.** Our parcellation approach included averaging the connectivity matrices across subjects. To ensure intersubject stability of these connectivity patterns, we performed a leave-one-out stability analysis. Specifically, we averaged the connectivity matrixes for  $N - 1$  subjects and computed the correlation between this averaged connectivity pattern and the connectivity pattern of the left-out subject for each OFC voxel. This was repeated  $N$  times, each time with a different subject as the left-out subject. The voxelwise correlation maps were then averaged across leave-one-out steps to obtain the average stability map.

**Stability of cluster solutions—variation of information metric.** To estimate the stability of the cluster solutions, we used the “variation of information” (VI) metric (Meila, 2007), which has previously been used to assess the stability of connectivity-based parcellations (Kelly et al., 2010). For this, we used a split-half comparison procedure. We randomly assigned subjects to one of two groups ( $N = 7$  and  $N = 6$ , respectively), averaged the connectivity matrices within each group, and computed the clustering for each group and each  $K$  ( $K = 2, 3 \dots 10$ ). We then compared the clustering of group one ( $C$ ) to the clustering of group two ( $C'$ ) within each  $K$  using the VI metric according to:

$$VI(C, C')_K = H(C)_K + H(C')_K - 2I(C, C')_K,$$

where  $H(C)_K$  and  $H(C')_K$  are the entropies (i.e., the amount of information) of clustering  $C$  and  $C'$ , respectively, and  $I(C, C')_K$  is the mutual information between the two clusterings  $C$  and  $C'$  (i.e., how

much information one clustering gives about the other).  $I(C, C')_K$  and  $H(C)_K$  are computed according to:

$$I(C, C')_K = \sum_{k=1}^K \sum_{k'=1}^{K'} P(k, k') \cdot \log \frac{P(k, k')}{P(k)P(k')},$$

and

$$H(C)_K = - \sum_{k=1}^K P(k) \cdot \log P(k).$$

$P(k)$  is the probability that a voxel belongs to cluster  $k$  and  $P(k, k')$  is the probability that a voxel belongs to cluster  $k$  in  $C$  and cluster  $k'$  in  $C'$ .  $P(k)$  and  $P(k, k')$  are computed according to:

$$P(k) = \frac{n_k}{n},$$

and

$$P(k, k') = \frac{|C_k \cap C'_k|}{n},$$

where  $n_k$  is the number of voxels in cluster  $k$ , and  $n$  is the total number of OFC voxels. Low VI values indicate high similarity between the two clusterings (and thus high stability), whereas high VI values indicate low similarity (and thus low stability). In total, this procedure was repeated 100 times, each time with new random split-half groups. Average VI values across split halves were then plotted as a function of  $K$ .

The average VI metric as a function of  $K$  can also serve as a marker for identifying the optimal  $K$  (Kelly et al., 2010). Specifically, a possible criterion for optimality is the stability and parsimony of cluster solutions. We defined the optimal  $K$  such that it is the smallest (i.e., most parsimonious)  $K$  for which its corresponding VI is statistically indistinguishable from that of the  $K - 1$  solution. In other words, optimality is given for the smallest  $K$  for which stability does not substantially decrease relative to  $K - 1$ .

**Symmetry index.** To quantify the symmetry of the cluster solutions between the two hemispheres, we computed a symmetry index,  $SI_K$ , for each cluster solution  $K > 1$ . This index reflects the percentage overlap between clusters on both hemispheres if one hemisphere is mirrored at the midline.  $SI_K$  is computed according to:

$$SI_K = \frac{1}{n} \sum_{v=1}^n \begin{cases} 1 & \text{if } x_v = x'_v \\ 0 & \text{otherwise} \end{cases},$$

where  $n$  is the number of voxels in one hemisphere, and  $x$  and  $x'$  are the cluster labels of voxel  $v$  in the original and mirrored cluster solution, respectively. Because this measure requires that the OFC ROI is mirror symmetric (i.e., that each voxel exists on both hemispheres), we only included voxels that are present on both sides and discarded voxels that are present on one side only. To test the empirically observed SI against chance, we computed the index  $10^6$  times based on random permutations of cluster labels for each  $K$ .

**Hierarchy index.** To quantify the hierarchical structure of our data, we computed a hierarchy index (HI) for each cluster solution  $K > 2$ . In brief, for a given  $K$  the index  $HI_K$  is inversely related to the number of parent clusters (calculated with  $K - 1$ ) each cluster (calculated with  $K$ ) has on average. We computed  $HI_K$  according to:

$$HI_K = \frac{1}{K} \sum_{i=1}^K \frac{\max_j(x_{ij})}{\bar{x}_i},$$

where  $\bar{x}_i = \sum_{j=1}^{K-1} x_{ij}$ , and for each  $K$ ,  $x$  is a matrix whose elements  $x_{ij}$  reflect the number of voxels in cluster  $j_i = 1 \dots K$  stemming from cluster  $j_j = 1 \dots K - 1$  in cluster solution  $K - 1$ . Given an ideal hierarchical structure, the step

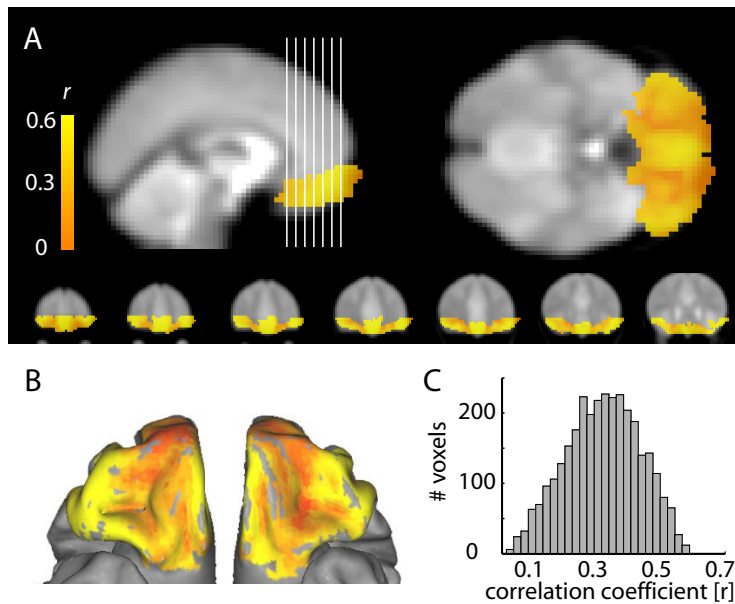


**Figure 2.** Intersubject stability of OFC connectivity patterns. **A**, Map of correlation coefficients depicting the average correlation between the OFC functional connectivity patterns (between activity in OFC and the rest of the brain) of all subjects (average leave-one-out correlation). Coronal sections on the bottom correspond to white vertical lines on the top left. **B**, Same stability map projected on the cortical surface. **C**, Histogram of correlation coefficients between the OFC connectivity patterns of different subjects.

from cluster solution  $K - 1$  to cluster solution  $K$  has an  $HI = 1$ , because all clusters in  $K$  stem from one, and only one, parent cluster in  $K - 1$ , as it is the case in the step from  $K = 1$  to  $K = 2$  (that is, the  $HI_2 = 1$ ). To test the empirically observed hierarchy index against chance, we computed the index  $10^6$  times based on random permutations of cluster labels for each  $K$ .

**Exploring the connectivity of OFC subdivisions.** To map and illustrate the functional connectivity profile of each OFC subdivision, we computed a subject-wise, first-level GLM for each cluster solution. These GLMs contained the averaged (across all within-cluster voxels, defined by the cluster label, regardless of hemisphere) time series from each OFC cluster as regressors (Chang et al., 2012). For instance, for the  $K = 2$  cluster solution the GLM contained (1) the averaged time series from all voxels belonging to cluster 1, and (2) the averaged time series from all voxels belonging to cluster 2. These time series were then regressed against the BOLD signal in each voxel (of the 3 mm set). Importantly, even though the time courses of the different clusters were only slightly correlated (average  $r = 0.136$ ), all regressors were simultaneously included in the GLM. By doing so, shared variance of different regressors is not attributed to any regressor, and the resulting parameter estimates for a single cluster (e.g., cluster 1) reflect the (partial) correlation between the activity in a given voxel and the activity in cluster 1, independent of activity in the other cluster (cluster 2). That is, this method identifies only regions in which activity is uniquely explained by the activity in one cluster. Single-subject contrast maps for each cluster were applied to second-level  $t$  tests to test for significant positive and negative connectivity at the group level. For all reported results, we used a threshold of  $p < 0.05$ , FWE whole-brain corrected.

## Results

### Stability of connectivity patterns

The intersubject stability of the OFC connectivity patterns was examined to (1) provide evidence for sufficient signal coverage in the OFC and (2) to demonstrate intersubject stability as a basis for averaging the individual connectivity matrices. Bad signal coverage in OFC would lead to small noise-driven correlations between the (noisy) resting-state signal in OFC and resting-state activity in the rest of the brain. These random connectivity pat-

terns would in turn lead to close-to-zero correlations between the connectivity patterns of different subjects. Furthermore, even with good signal coverage in the OFC, correlations between the connectivity patterns of different subjects would be close to zero if individual subjects had strong differences in the connectivity patterns of their OFCs. Thus, significant stability is only possible if (1) signal coverage is adequate and (2) the OFCs of different subjects are similarly connected to the rest of their brains.

The average stability of the functional connectivity patterns in the OFC was  $r = 0.32$ . The stability map is plotted in Figure 2 along with the distribution of correlation coefficients (Fig. 2C). It can be seen that high reliabilities were concentrated in the medial OFC (Fig. 2A,B). This is important to note because this ventromedial region is specifically susceptible to signal dropouts (Weiskopf et al., 2006). Lower stability was found in areas near the transverse orbital sulcus (TOS), medial orbital sulcus (MOS), olfactory sulcus, and the inferior frontal pole. Assuming individual differences in the exact gyral anatomy of

the OFC, low stability can be expected at sulci because there voxels are more likely to belong to different anatomical (and presumably connective) regions in different subjects, hence reducing the similarity of connectivity profiles in these voxels. However, the overall presence of similar connectivity profiles across subjects demonstrates sufficient signal coverage in the OFC and furthermore establishes the grounds to average the individual connectivity matrices.

### Connectivity based parcellation of OFC

We used an unsupervised  $K$ -means cluster algorithm to identify different parcellations of the OFC. Our clustering method was entirely based on the similarity in the functional connectivity profile between resting-state activity in the OFC and the rest of the brain. That is, the likelihood that two voxels are clustered together is higher the more similar their connectivity profiles.

The  $K = 2$  cluster solution (Fig. 3A) revealed one cluster (Fig. 3A, 1) covering the medial OFC including the ventromedial wall, the GR, the inferior medial gyrus (IMG), the superior medial gyrus (SMG), the MOG, the posterior part of the MOS, the posterior orbital gyrus, as well as the posterior part of the lateral orbital gyrus (LOG) including the horizontal ramus of the sylvian fissure (HR). The second cluster (2) covered the central and anterior-lateral part of the orbitofrontal surface, including the anterior orbital gyrus (AOG), the TOS, the lateral orbital sulcus (LOS) and the anterior part of the MOS. Importantly, the two clusters did not divide the left and the right hemisphere but, in contrast, were fairly symmetric in both hemispheres. That is, voxels across hemispheres are labeled more similarly than neighboring voxels in the same hemisphere. The topography of these two clusters clearly corresponds to the medial and orbital networks defined by Ongür and Price (2000) based on anatomical connections within the monkey OFC (for comparison, see their Fig. 5). This is important to note because it shows that at the simplest

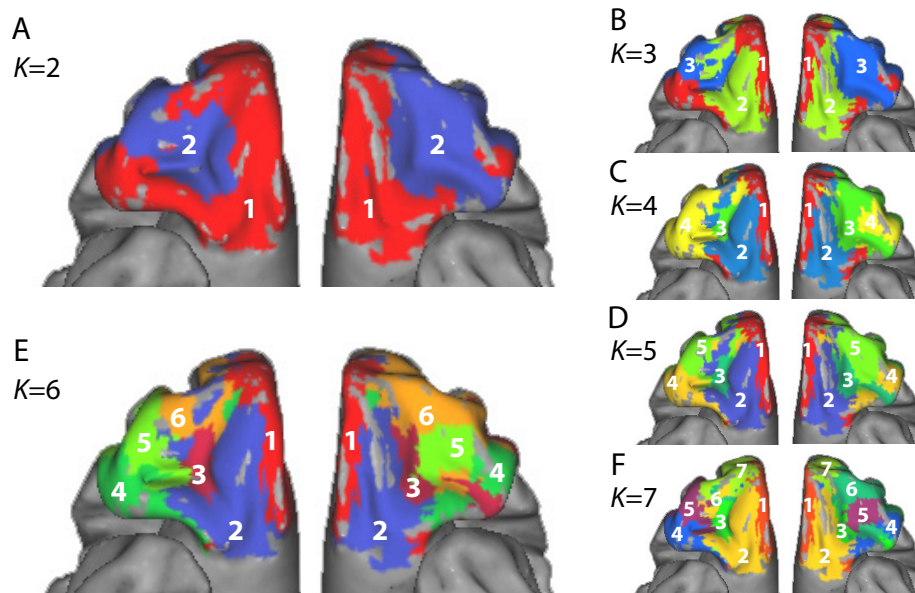


**Figure 3.** Connectivity-based parcellation of the human OFC. **A–F**, Cluster solutions with different  $K$  (2–7). See main text and Table 1 for a detailed description of the clusters.

level, our method is able to replicate a parcellation that has been found using different and more direct measures of connectivity.

Following this fundamental  $K = 2$  cluster solution, we proceed to present more detailed parcellations with more clusters that might provide a better account for OFC subdivisions. In particular, we computed further cluster solutions up to  $K = 10$  clusters. However, we only present results up to  $K = 7$  because solutions with more clusters tend to be asymmetric (i.e., have clusters that appear in only one hemisphere). Generally, most clusters consisted of two spatially continuous regions (one on the left and one on the right hemisphere), except for the medial/posterior–lateral cluster (1), which in the  $K = 3$  cluster solution had three main compartments, one located in the medial OFC and two in the posterior–lateral OFC (left and right hemisphere, respectively). However, some clusters also had voxels that were isolated from their main compartments, but these voxels were very infrequent. Table 1 contains the MNI coordinates of the centers of the clusters (arithmetic mean) for each  $K$ . The cluster maps in MNI space can be obtained from the corresponding author.

In the  $K = 3$  cluster solution (Fig. 3B), one cluster (1) covered the medial wall of the OFC (including the GR, the IMG, and the SMG) as well as the posterior–lateral surface (including the LOG and the HR). A second cluster (2) covered the posterior–central surface (including the MOS and the MOG), and a third cluster (3) the central and anterior–lateral part of the OFC (including the TOS, the LOS, and the AOG). The  $K = 5$  cluster solution (Fig. 3D) also revealed the same medial (1) and posterior–central cluster (2). Furthermore, a cluster covering the very central part of the orbitofrontal surface (3) at the medial intersection between the TOS and the MOS and a part of the left HR emerged. The lateral OFC split along the anterior–posterior axis into a posterior–lateral (4, including the LOG, the posterior LOS and HR) and an anterior–lateral cluster (5, including the AOG and the anterior LOS). In the  $K = 6$  and  $K = 7$  cluster solutions (Fig. 3E,F), the medial (1), the posterior–central (2), and the central (3) clusters were conserved. The lateral part, however, split into more and more clusters, suggesting a connective and presumably func-

**Table 1.** MNI coordinates of  $k$  cluster centers for  $K = 1$ –7

$K$ -cluster solution	$k$	Left hemisphere			Right hemisphere		
		$x$	$y$	$z$	$x$	$y$	$z$
2	1	−17	42	−13	11	41	−15
	2	−36	44	−10	33	42	−9
3	1	−17	44	−12	9	46	−13
	2	−21	37	−18	16	31	−18
	3	−39	46	−8	34	42	−9
4	1	−8	47	−12	7	47	−13
	2	−20	36	−18	16	31	−18
	3	−28	38	−11	34	42	−8
5	4	−40	43	−9	38	38	−13
	1	−7	48	−12	6	47	−13
	2	−19	35	−18	16	29	−19
	3	−29	36	−12	36	32	−8
6	4	−43	31	−11	39	31	−14
	5	−37	52	−8	30	52	−9
	1	−7	49	−12	6	47	−13
	2	−19	35	−19	16	28	−19
	3	−26	36	−13	37	32	−8
7	4	−43	30	−11	40	31	−14
	5	−42	46	−8	31	39	−12
	6	−28	57	−8	28	54	−8
	1	−6	47	−12	5	45	−13
	2	−19	31	−20	16	27	−20
	3	−26	36	−13	37	32	−7
	4	−43	29	−11	41	30	−14
5	−42	47	−8	31	38	−13	
6	−29	53	−8	32	48	−9	
7	−21	61	−9	13	64	−9	

The  $x$ ,  $y$ , and  $z$  coordinates in MNI space for the center (arithmetic mean) of each cluster  $k$  in each cluster solution  $K$ . Although the clustering was performed on voxels from both hemispheres simultaneously, cluster centers are reported for the left and right hemisphere separately.

tional specialization in lateral OFC. Specifically, in the  $K = 6$  cluster solution (Fig. 3E) the lateral part split along the anterior–posterior axis into a posterior–lateral (4), a mid-lateral (5), and an anterior–lateral (6) cluster. This detailed and symmetric clustering suggests that the  $K = 2$  cluster solution may provide an overly simplistic account of OFC subdivisions and that finer par-

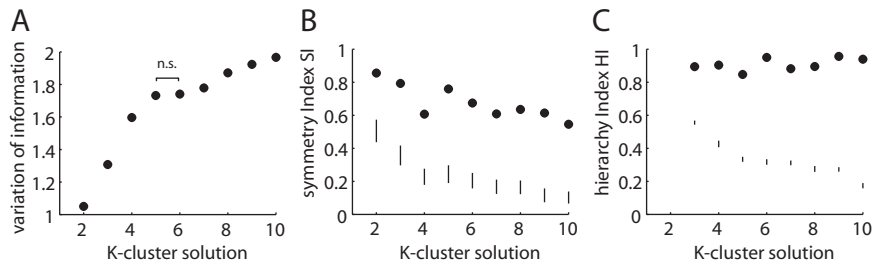


**Figure 4.** Stability, symmetry, and hierarchy of cluster solutions. **A**, VI based on a split-half reliability analysis (100 random split halves) as a function of  $K$ . High VI indicates low stability. All VIs of different  $K$ s are significantly ( $p < 0.0001$ ) different except for the difference between  $K = 5$  and  $K = 6$  ( $t = 0.70$ ,  $p = 0.49$ ). Thus,  $K = 6$  is the optimal  $K$  because it is the smallest  $K$  in which stability does not decrease relative to  $K - 1$ . Error bars for SEM are smaller than the symbols. **B**, SI as a function of  $K$ . SI reflects the percentage of equally labeled voxels in the left and right hemisphere, when mirrored at the midline. Black dots depict empirical SI, and black vertical lines depict the range of SI values based on  $10^6$  permutations of random cluster labeling. **C**, HI as a function of  $K$ , reflecting the hierarchical structure of the different solutions by the average probability that a given cluster in  $K$  has only one "parent-cluster" in  $K - 1$ . Perfect hierarchy results in HI = 1. Black dots depict empirical HI, and black vertical lines depict the range of HI values based on  $10^6$  permutations of random cluster labeling.

cellations may be better suited to appropriately characterize OFC subdivisions.

### Stability of cluster solutions—finding the optimal $K$

We assessed the stability of the different cluster solutions using the VI metric (Meila, 2007) and a random split-half comparison procedure for  $K = 2 \dots 10$  cluster solutions. For each  $K$ , we compared the cluster solutions generated based on the averaged connectivity matrices of two random split-half groups of subjects. Across the 100 randomly selected split-half groups, the similarity (i.e., stability) decreased (increasing VI) as a function of  $K$  (Fig. 4A) and was comparable to the stability of previously reported cluster solutions (Kelly et al., 2010). VI significantly increased with nearly every  $K$  (all  $p$  values  $< 0.0001$ ). Only the VIs from the  $K = 5$  and  $K = 6$  cluster solutions were statistically indistinguishable ( $t = 0.70$ ,  $p = 0.49$ ). Accordingly, the  $K = 6$  cluster solution is optimal in the sense that it is the smallest (i.e., most parsimonious)  $K$  for which VI does not significantly increase relative to  $K - 1$ .

### Symmetry of cluster solutions

One important feature of the reported cluster solutions is their apparent symmetry across hemispheres. For example, all clusters up to the  $K = 7$  cluster solution appeared on both sides, and the  $K = 8$  cluster solution was the first solution in which one cluster was found only in one hemisphere. To quantify the symmetry of each cluster solution, we mirrored the topographies at the midline and computed a measure of symmetry SI (see Materials and Methods). This index reflects the percentage overlap between cluster labels in both hemispheres. The SI for the different cluster solutions is plotted in Figure 4B, along with the range of SIs from  $10^6$  random permutations of cluster labels. It can be seen that most cluster solutions had  $>60\%$  correspondence between the left and right hemispheres, and none of the random permutations exceeded the empirical SI. This shows that the connectivity-based cluster solutions are fairly similar in both hemispheres. This finding provides important face validity for our clustering because cluster solutions based on mere distance relations (and thus noise) cannot be expected to unfold symmetrically.

### Hierarchical structure of cluster solutions

Qualitatively, the different cluster solutions seem to be organized in a fairly hierarchical manner. That is, with each new cluster,

only one cluster from  $K - 1$  splits up into two new clusters in  $K$ . To quantitatively test this impression, we computed an HI for each cluster solution (see Materials and Methods). This index reflects the average (across clusters) percentage of voxels in a cluster in  $K$  that stemmed from only one parent cluster. In Figure 4C, HI is plotted as a function of  $K$ , along with the range of HI values from  $10^6$  random permutations of cluster labels. On average, 90% of voxels in each cluster of the  $K$ -cluster solution stemmed from only one cluster in the  $K - 1$  cluster solution, providing good evidence for a hierarchical organization of the OFC subdivisions.

Furthermore, it can be seen that none of the  $10^6$  random permutations resulted in an HI that was higher than that empirically observed. It is important to note that all cluster solutions were computed independently, and our clustering algorithm did not privilege hierarchical solutions as do alternative algorithms (e.g., hierarchical clustering).

### Resting-state connectivity of OFC subdivisions

So far, we have shown that robust and symmetric subdivisions of the OFC can be revealed based on the functional connectivity profile with the rest of the brain. In the following exploratory analyses, we in turn map the brain regions in which activity significantly ( $p < 0.05$ , FWE whole-brain corrected) co-fluctuates with activity in different OFC clusters. Importantly, given that the clustering was based on homogeneous functional connectivity profiles, it is not a question of whether these clusters are functionally connected to different brain regions, but rather which brain regions these are. Furthermore, it should be noted that our measure of functional connectivity relies on co-fluctuations in resting-state fMRI activity, and it is not yet clear how this measure is related to anatomical long-range connections (Van Dijk et al., 2010).

The medial/posterior–lateral cluster (1, red) of the  $K = 2$  cluster solution was functionally connected to the superior frontal gyrus (BA 8/9), the inferior parietal cortex (PC) (BA 39) and the anterior part of the middle and inferior temporal cortex (TC) (BA 20/21) (Fig. 5B). On the medial surface, this cluster showed positive functional connectivity with the posterior cingulate cortex/precuneus (PCC) (BA 23) and the entire medial PFC [BA 10/32/9, except for the anterior cingulate cortex (ACC) (BA 24/25)], extending into the ventromedial striatum (Fig. 5C). Furthermore, we found positive functional connectivity to regions in the parahippocampal gyrus (BA 28/34) and adjacent temporal pole (BA 38) (Fig. 5D). Negative functional connectivity of the medial/posterior–lateral cluster (Fig. 5E–G) was found with the middle frontal gyrus (BA 45/46), the anterior insular (AI) and adjacent frontal operculum, the inferior PC (BA 40), as well as the inferior TC (BA 37). The anterior–lateral cluster (2, blue) showed positive functional connectivity with the inferior and the middle frontal gyrus (BA 9/45/46), the inferior PC (BA 39), as well as the inferior temporal gyrus (BA 20/37) (Fig. 5B). Interestingly, the regions in the TC are posterior to those correlated with the medial/posterior–lateral OFC cluster (Fig. 5B). Furthermore, we found positive functional connectivity with a region in the medial superior frontal gyrus (medial BA 8) (Fig.

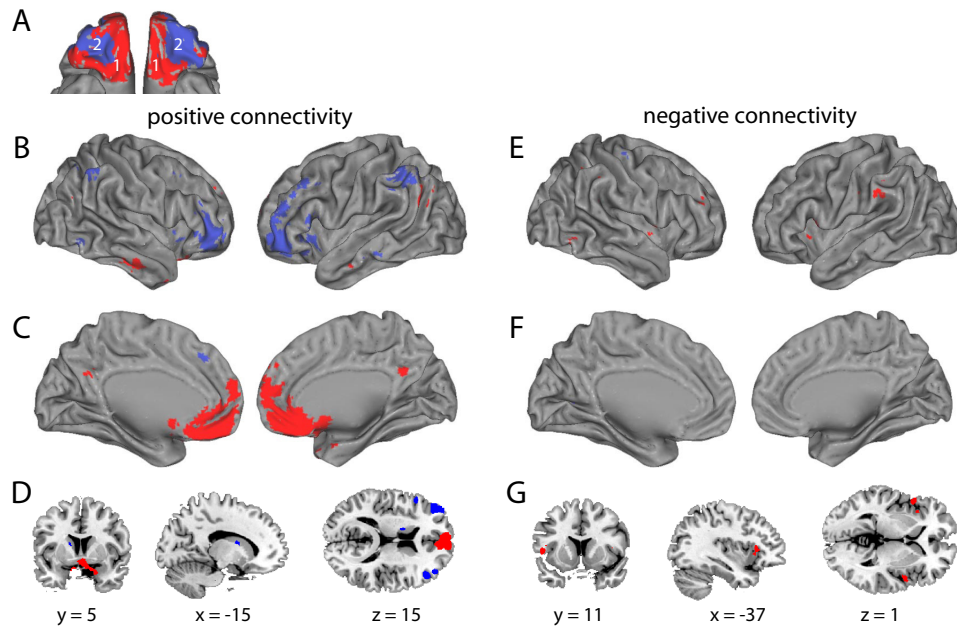


**Figure 5.** Functional connectivity of OFC subdivisions in the  $K = 2$  cluster solution. **A**, Color code of different OFC subdivisions. **B**, Positive resting-state connectivity of different subdivisions with regions on the right (left) and left (right) lateral surface. **C**, Positive resting-state connectivity of different subdivisions with regions on the right (right) and left (left) medial surface. **D**, Positive resting-state connectivity of different subdivisions with subcortical regions depicted in coronal (left), sagittal (middle), and transversal (right) sections. Coordinates on the bottom refer to MNI space. **E–G**, Negative resting-state connectivity of different OFC subdivisions with cortical and subcortical structures. T-maps of resting-state connectivity are thresholded at  $p < 0.05$ , FWE whole-brain corrected.

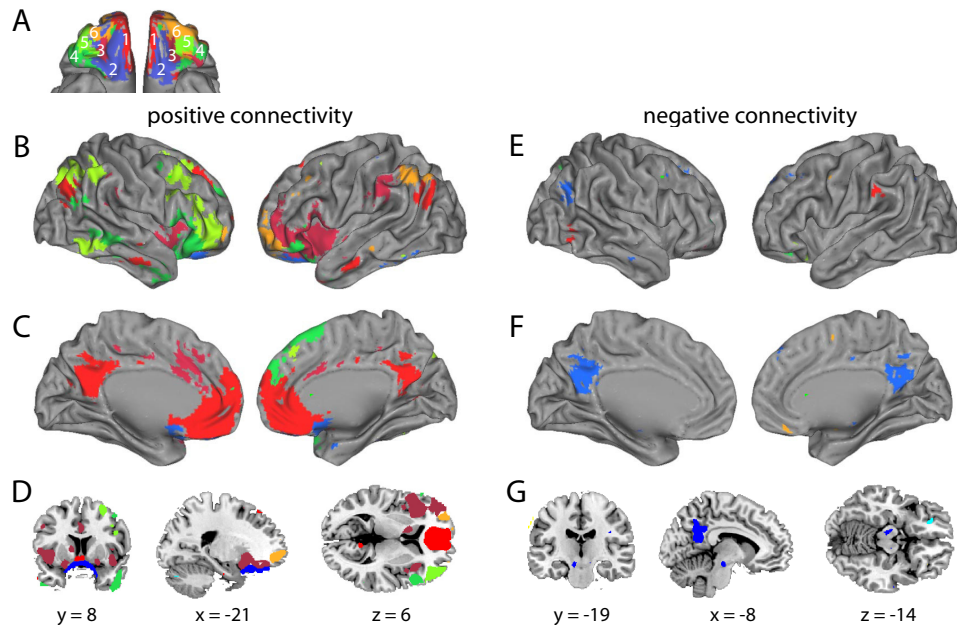


**Figure 6.** Functional connectivity of OFC subdivisions in the  $K = 6$  cluster solution. **A**, Color code of different OFC subdivisions. **B–D**, Positive resting-state connectivity of different subdivisions with cortical and subcortical structures. **E–G**, Negative resting-state connectivity of different OFC subdivisions with cortical and subcortical structures. Coordinates on the bottom refer to MNI space. T-maps of resting-state connectivity are thresholded at  $p < 0.05$ , FWE whole-brain corrected.

5C) and the dorsal striatum (caudate head) (Fig. 5D). We identified only small regions with negative functional connectivity in the precentral gyrus (BA 4) (Fig. 5E).

In contrast to the functional connectivity profile of the coarse twofold parcellation described above, the “optimal”  $K = 6$  cluster solution revealed a much more detailed and segmented pattern of functional connectivity involving partly different brain regions (Fig. 6). Here, the medial OFC cluster (1, red) showed positive

functional connectivity with the inferior PC (BA 39), the anterior middle and inferior temporal gyrus (BA 20/21), the superior frontal gyrus (BA 9) (Fig. 6B), as well as the medial PFC (BA 10/32) and PCC (BA 23) (Fig. 6C). We also observed positive functional connectivity with the medial TC (BA 36) (Fig. 6D) and the temporal pole (BA 20/38), and negative functional connectivity to the left inferior PC (BA 40) and TC (BA 37) (Fig. 6E). We found positive functional connectivity of the posterior–central

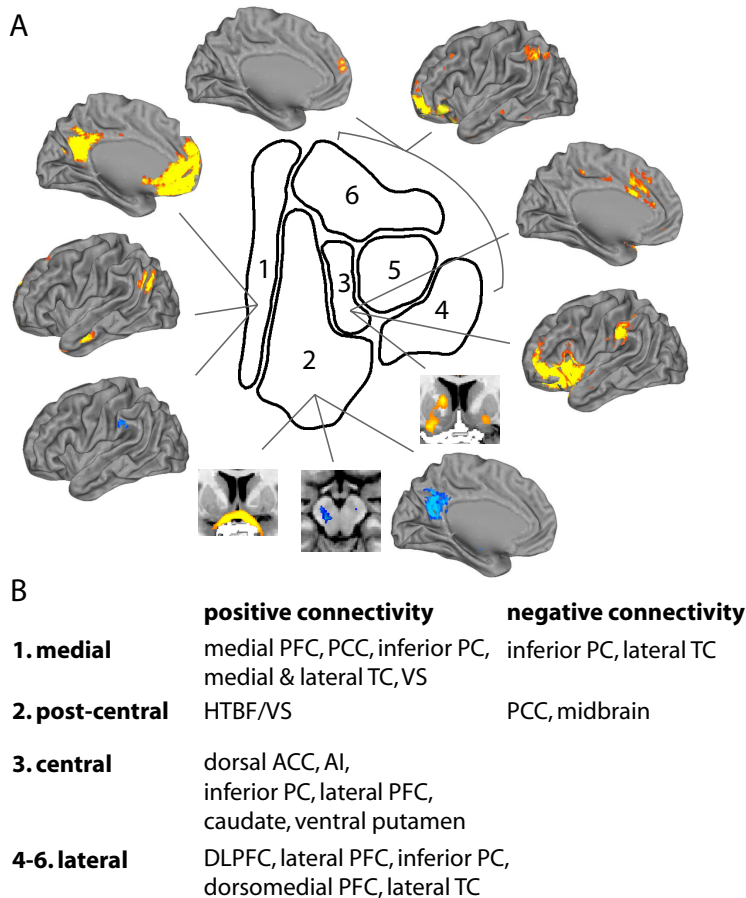


**Figure 7.** Summary of OFC subdivisions and functional connectivity profiles. **A**, Schematic view of connectivity based OFC subdivisions (based on the optimal  $K = 6$  cluster solution) along with their connectivity profile to other brain regions. Only the left hemisphere is shown. Regions showing functional connectivity ( $p < 0.05$ , FWE corrected) with these clusters are depicted on the surface plots and the sections. **B**, List of regions to which clusters show functional connectivity. HTBF/VS, Hypothalamic basal forebrain/ventral striatum.

cluster (2, blue) with the hypothalamic basal forebrain extending into the ventral striatum (Fig. 6C) and the parahippocampal gyrus (BA 28). Negative functional connectivity (Fig. 6E–G) was found with the PCC (BA 23), the middle and superior frontal gyrus (BA 8/9), the inferior PC (BA 39), and the bilateral midbrain (Fig. 6G). The central OFC cluster (3, purple) exhibited functional connectivity with the AI extending into the left ventrolateral PFC (BA 45/46) as well as the inferior PC (BA 40) (Fig. 6B). On the medial surface, this cluster showed functional connectivity with the dorsal ACC (BA 24/32) (Fig. 6C), and subcortically with the dorsal (caudate head) and the ventral striatum (ventrolateral putamen) (Fig. 6D). The three lateral clusters spanning an anterior–posterior gradient (posterior–lateral 4, mid-lateral 5, and anterior–lateral 6, in dark green, bright green, and orange, respectively) showed positive functional connectivity with adjacent regions in the inferior PC (BA 39/40); the superior, middle, and inferior frontal gyrus; as well as the middle and inferior TC (BA 20/21/37) (Fig. 6B,D). Furthermore, the posterior–lateral and mid-lateral clusters showed functional connectivity with dorsomedial frontal areas, including the medial superior frontal gyrus (BA 8/9) and the supplementary motor area (BA 6) (Fig. 6C).

In summary, the following patterns of functional connectivity were found for the optimal  $K = 6$  cluster solution (Fig. 7). The medial cluster (1) was functionally connected to the

medial PFC and medial PCC; the posterior–central cluster (2) showed negative functional connectivity to the PCC and the midbrain; the central cluster (3) showed negative functional connectivity to the AI, inferior PC, the dorsal ACC and the striatum; whereas the lateral clusters (4–6) showed functional connectivity to adjacent regions in the lateral PFC as well as regions in the inferior PC and the lateral TC.

## Discussion

In the current study, we applied an unsupervised clustering technique to resting-state fMRI data to parcellate the human OFC based on shared functional connectivity profiles with the rest of the brain. We found robust, detailed, and symmetric subdivisions of the human OFC. Moreover, subsequently adding new clusters revealed a hierarchical clustering structure. This hierarchical organization, especially in the lateral OFC, suggests the existence of rather broadly defined functional regions in the OFC, which themselves contain finer, functionally specialized subdivisions.

Previous attempts to parcellate the monkey OFC based on anatomical connections revealed an orbital and a medial network (Carmichael and Price, 1996; Ongür and Price, 2000). These two networks were defined based on the intraregional anatomical connections within the OFC and are thus only modestly interconnected. Interestingly, they also share only a few connections to the rest of the brain.

Specifically, the orbital network, covering the central and anterior–lateral surface, receives mainly input from higher sensory areas and projects to lateral striatal areas (Ferry et al., 2000). The medial network, covering the medial as well as posterior–lateral OFC, is extensively connected to the hypothalamus and the medial PFC (which is part of the medial network in this terminology) and projects to medial areas of the striatum (Ferry et al., 2000). Importantly, although this twofold partition in monkeys is based on structural connectivity (i.e., intraregional anatomical connections within the OFC), it nevertheless clearly corresponds to our  $K = 2$  cluster solution. However, in addition to this twofold parcellation schema, our data suggest that the human OFC may exhibit an even finer connective organization.

Specifically, according to our data, the OFC consists of six subdivisions with homogeneous functional connectivity profiles: (1) the medial OFC; (2) the posterior–central OFC; (3) the central OFC; and (4–6) three clusters in the lateral OFC along the anterior–posterior gradient (see Fig. 7). The medial OFC cluster was functionally connected to the medial PFC, the PCC, the ventral striatum, the lateral PC, and regions in the lateral and medial TC. The posterior–central OFC cluster showed primarily negative functional connectivity (negative correlation in resting-state activity) with the PCC and the midbrain. The central OFC cluster showed widespread functional connectivity with the AI, the lateral PFC and lateral PC, the dorsal ACC, as well as the dorsal and ventrolateral striatum. Finally,

the clusters in the lateral OFC showed positive functional connectivity to areas in the lateral and dorsolateral PFC (DLPFC), the lateral PC, and the lateral TC.

These results, revealed using cofluctuations in resting-state fMRI signals, are broadly consistent with results from tracing studies in nonhuman primates (Cavada et al., 2000; Ongür and Price, 2000). Specifically, the primate OFC is anatomically connected to the lateral and dorsolateral PFC (Barbas and Pandya, 1989; Carmichael and Price, 1995b), the PC (Cavada and Goldman-Rakic, 1989a,b; Morecraft et al., 1992), as well as the AI and the TC (Mesulam and Mufson, 1982a,b; Mufson and Mesulam, 1982). Anatomical connections to structures in the medial temporal lobe (Carmichael and Price, 1995a; Ongür and Price, 2000), the midbrain (Porrino and Goldman-Rakic, 1982; Williams and Goldman-Rakic, 1998), and the striatum (Ferry et al., 2000) are also well documented.

The human OFC has been parcellated into several subdivisions based on its cytoarchitecture by Mackey and Petrides (2010) and Ongür et al. (2003). These two systems are not in perfect agreement, but both suggest a more detailed parcellation of the OFC than just a medial–lateral distinction. Although there is not a direct 1:1 mapping between our connectivity-based parcellation and these cytoarchitectonic divisions, the identified clusters can be described in terms of cytoarchitectonic regions. The medial cluster covers areas labeled as 11m, 14r, and 14c, which (together with the medial part of area 13) also fall in the posterior–central cluster. The central cluster lies between areas 11 and 13. Interestingly, the lateral clusters can be approximately mapped onto areas 47/12o, 47/12m, and (anterior) 11 in the system of Mackey and Petrides (2010).

The distinct functional connectivity patterns of the OFC subdivisions are likely to be paralleled by specific functional roles. Previous studies have proposed a simple medial–lateral functional distinction of the OFC (O'Doherty et al., 2001; Kringlebach and Rolls, 2004). Although we observed some support for this distinction in our two-cluster solution, our data suggest a finer connectional and presumably functional segregation. Human neuroimaging studies have found representations of expected reward and decision values in the region belonging to the medial cluster (Hare et al., 2009; Kahnt et al., 2011b; Kim et al., 2011; Park et al., 2011), which in our study was mainly connected to the medial PFC and PCC. These regions are themselves associated with reward but also with episodic memory and self-related processes (Cavanna and Trimble, 2006; Sajonz et al., 2010). The posterior–central cluster showed negative connectivity to a well defined region in the midbrain, possibly corresponding to the substantia nigra. In primates, dopaminergic neurons in this area innervate the striatum and the OFC (Lynd-Balta and Haber, 1994; Williams and Goldman-Rakic, 1998), and code a key signal for reward learning, the reward prediction error (Schultz et al., 1997), suggesting a role for this OFC subdivision in reward learning. The central cluster exhibited connections to the ventrolateral and dorsal striatum that are involved in learning the value of stimuli and actions, respectively (O'Doherty et al., 2004; Balleine et al., 2007; Kahnt et al., 2009). Interestingly, this cluster was also connected to executive regions in the dorsomedial frontal cortex that have been linked to representing and updating action values (Behrens et al., 2007; Gläscher et al., 2009), suggesting a role for this subdivision in decision making. Finally, the lateral clusters were connected to regions in the TC and PC, representing highly processed visual information, but also to the DLPFC, which is involved in regulating value representations (Delgado et al., 2008; Hare et al., 2009). Sensory and regulatory

input may modulate reward representations, learning, and choices via these pathways.

There are potential limitations that should be considered when interpreting our results. Despite its widespread use (Fox and Raichle, 2007; Biswal et al., 2010), the precise relationship between our measure of functional connectivity based on cofluctuations in resting-state fMRI activity and anatomical connections remains unclear. Spontaneous fluctuations in the BOLD signal have been used to uncover functional brain networks (Biswal et al., 1995; Fox and Raichle, 2007) and appear to reflect but are not limited to anatomical connections in monkeys (Vincent et al., 2007; Margulies et al., 2009) and humans (Zhang et al., 2008). Furthermore, resting-state connectivity has been demonstrated to preserve the detailed and topographically organized anatomical connections between V1 and V3 (Heinzle et al., 2011), suggesting that this method can detect meaningful anatomical connections. Future work should compare and contrast our OFC parcellation with more direct measures of anatomical connectivity using techniques such as diffusion tensor imaging (Johansen-Berg and Rushworth, 2009).

Previous work has shown that tasks performed directly before resting-state data collection increase task-specific functional connections (Stevens et al., 2010). Our resting-state data were acquired after a ~1 h reward-based task (Kahnt et al., 2011a) and ~10 min of anatomical scans. Although increases in reward-specific connections could increase the likelihood of revealing robust parcellations of the OFC, they should have little effect on the exact borders of the identified clusters. However, the prior reward-based task (although separated from the resting-state session by a ~10 min break) could have led to a more robust parcellation compared with a resting-state scan without this prior task.

The orbitofrontal cortex is highly susceptible to fMRI signal dropouts, and noisy signal may have potentially affected our clustering results. However, we believe this is unlikely for several reasons. First, we found considerable stability of the connectivity patterns across subjects, especially in medial areas, where signal dropout has previously been reported. Importantly, this stability requires good signal coverage as a necessary condition. Second, visual inspection of the EPIs demonstrated adequate coverage in all regions of the OFC. Third, although we placed no anatomical constraints on the clustering algorithm, clusters were highly symmetric across the two hemispheres, implying that the cluster solutions did not depend on pure distance relations between individual OFC voxels. Fourth, we observed clear connectivity profiles of OFC subdivisions with voxels in the rest of the brain, which is unlikely if OFC signal is mainly driven by noise due to bad coverage.

In conclusion, we have shown that detailed, symmetric, and hierarchically organized OFC subdivisions can be defined based on their shared patterns of connectivity with the rest of the brain. Although our approach replicated a twofold parcellation previously described in monkeys, further analyses supported a finer, sixfold parcellation of the OFC. Moreover, the distinct connectivity patterns of these clusters are suggestive of specific functional roles of these subdivisions for reward processing, learning, and decision making. Using this parcellation as a reference for reporting localization results in future fMRI studies will be useful for advancing our understanding of OFC function.

## References

- Balleine BW, Delgado MR, Hikosaka O (2007) The role of the dorsal striatum in reward and decision-making. *J Neurosci* 27:8161–8165.

- Barbas H, Pandya DN (1989) Architecture and intrinsic connections of the prefrontal cortex in the rhesus monkey. *J Comp Neurol* 286:353–375.
- Beckmann M, Johansen-Berg H, Rushworth MF (2009) Connectivity-based parcellation of human cingulate cortex and its relation to functional specialization. *J Neurosci* 29:1175–1190.
- Behrens TE, Woolrich MW, Walton ME, Rushworth MF (2007) Learning the value of information in an uncertain world. *Nat Neurosci* 10:1214–1221.
- Biswal BB, Mennes M, Zuo XN, Gohel S, Kelly C, Smith SM, Beckmann CF, Adelstein JS, Buckner RL, Colcombe S, Dogonowski AM, Ernst M, Fair D, Hampson M, Hoptman MJ, Hyde JS, Kiviniemi VJ, Kötter R, Li SJ, Lin CP, et al (2010) Toward discovery science of human brain function. *Proc Natl Acad Sci U S A* 107:4734–4739.
- Biswal B, Yetkin FZ, Haughton VM, Hyde JS (1995) Functional connectivity in the motor cortex of resting human brain using echo-planar MRI. *Magn Reson Med* 34:537–541.
- Brodmann K (1909) Vergleichende lokalisationslehre der grosshirnrinde: in ihren principien dargestellt auf grund des zellenbaues. Leipzig, Germany: Johann Ambrosius Barth Verlag.
- Carmichael ST, Price JL (1994) Architectonic subdivision of the orbital and medial prefrontal cortex in the macaque monkey. *J Comp Neurol* 346:366–402.
- Carmichael ST, Price JL (1995a) Limbic connections of the orbital and medial prefrontal cortex in macaque monkeys. *J Comp Neurol* 363:615–641.
- Carmichael ST, Price JL (1995b) Sensory and premotor connections of the orbital and medial prefrontal cortex of macaque monkeys. *J Comp Neurol* 363:642–664.
- Carmichael ST, Price JL (1996) Connectional networks within the orbital and medial prefrontal cortex of macaque monkeys. *J Comp Neurol* 371:179–207.
- Cauda F, D'Agata F, Sacco K, Duca S, Geminiani G, Vercelli A (2011) Functional connectivity of the insula in the resting brain. *Neuroimage* 55:8–23.
- Cavada C, Goldman-Rakic PS (1989a) Posterior parietal cortex in rhesus monkey: I. Parcellation of areas based on distinctive limbic and sensory corticocortical connections. *J Comp Neurol* 287:393–421.
- Cavada C, Goldman-Rakic PS (1989b) Posterior parietal cortex in rhesus monkey: II. Evidence for segregated corticocortical networks linking sensory and limbic areas with the frontal lobe. *J Comp Neurol* 287:422–445.
- Cavada C, Compañy T, Tejedor J, Cruz-Rizzolo RJ, Reinoso-Suárez F (2000) The anatomical connections of the macaque monkey orbitofrontal cortex. A review. *Cereb Cortex* 10:220–242.
- Cavanna AE, Trimble MR (2006) The precuneus: a review of its functional anatomy and behavioural correlates. *Brain* 129:564–583.
- Chang LJ, Yarkoni T, Khaw MW, Sanfey AG (2012) Decoding the role of the insula in human cognition: functional parcellation and large-scale reverse inference. *Cereb Cortex*. Advance online publication. Retrieved March 28, 2012. doi:10.1093/cercor/bhs065.
- Chiavaras MM, Petrides M (2000) Orbitofrontal sulci of the human and macaque monkey brain. *J Comp Neurol* 422:35–54.
- Cohen AL, Fair DA, Dosenbach NU, Miezin FM, Dierker D, Van Essen DC, Schlaggar BL, Petersen SE (2008) Defining functional areas in individual human brains using resting functional connectivity MRI. *Neuroimage* 41:45–57.
- Delgado MR, Gillis MM, Phelps EA (2008) Regulating the expectation of reward via cognitive strategies. *Nat Neurosci* 11:880–881.
- Eickhoff SB, Bzdok D, Laird AR, Roski C, Caspers S, Zilles K, Fox PT (2011) Co-activation patterns distinguish cortical modules, their connectivity and functional differentiation. *Neuroimage* 57:938–949.
- Elliott R, Dolan RJ, Frith CD (2000) Dissociable functions in the medial and lateral orbitofrontal cortex: evidence from human neuroimaging studies. *Cereb Cortex* 10:308–317.
- Ferry AT, Ongür D, An X, Price JL (2000) Prefrontal cortical projections to the striatum in macaque monkeys: evidence for an organization related to prefrontal networks. *J Comp Neurol* 425:447–470.
- Fox MD, Raichle ME (2007) Spontaneous fluctuations in brain activity observed with functional magnetic resonance imaging. *Nat Rev Neurosci* 8:700–711.
- Fox MD, Zhang D, Snyder AZ, Raichle ME (2009) The global signal and observed anticorrelated resting state brain networks. *J Neurophysiol* 101:3270–3283.
- Gläscher J, Hampton AN, O'Doherty JP (2009) Determining a role for ventromedial prefrontal cortex in encoding action-based value signals during reward-related decision making. *Cereb Cortex* 19:483–495.
- Gottfried JA, O'Doherty J, Dolan RJ (2003) Encoding predictive reward value in human amygdala and orbitofrontal cortex. *Science* 301:1104–1107.
- Hare TA, Camerer CF, Rangel A (2009) Self-control in decision-making involves modulation of the vmPFC valuation system. *Science* 324:646–648.
- Heinzle J, Kahnt T, Haynes JD (2011) Topographically specific functional connectivity between visual field maps in the human brain. *Neuroimage* 56:1426–1436.
- Johansen-Berg H, Rushworth MF (2009) Using diffusion imaging to study human connective anatomy. *Annu Rev Neurosci* 32:75–94.
- Johansen-Berg H, Behrens TE, Robson MD, Drobjak I, Rushworth MF, Brady JM, Smith SM, Higham DJ, Matthews PM (2004) Changes in connectivity profiles define functionally distinct regions in human medial frontal cortex. *Proc Natl Acad Sci U S A* 101:13335–13340.
- Kahnt T, Park SQ, Cohen MX, Beck A, Heinz A, Wrase J (2009) Dorsal striatal-midbrain connectivity in humans predicts how reinforcements are used to guide decisions. *J Cogn Neurosci* 21:1332–1345.
- Kahnt T, Heinzle J, Park SQ, Haynes JD (2010) The neural code of reward anticipation in human orbitofrontal cortex. *Proc Natl Acad Sci U S A* 107:6010–6015.
- Kahnt T, Heinzle J, Park SQ, Haynes JD (2011a) Decoding different roles for vmPFC and dlPFC in multi-attribute decision making. *Neuroimage* 56:709–715.
- Kahnt T, Heinzle J, Park SQ, Haynes JD (2011b) Decoding the formation of reward predictions across learning. *J Neurosci* 31:14624–14630.
- Kelly C, Uddin LQ, Shehzad Z, Margulies DS, Castellanos FX, Milham MP, Petrides M (2010) Broca's region: linking human brain functional connectivity data and non-human primate tracing anatomy studies. *Eur J Neurosci* 32:383–398.
- Kim H, Shimojo S, O'Doherty JP (2011) Overlapping responses for the expectation of juice and money rewards in human ventromedial prefrontal cortex. *Cereb Cortex* 21:769–776.
- Kim JH, Lee JM, Jo HJ, Kim SH, Lee JH, Kim ST, Seo SW, Cox RW, Na DL, Kim SI, Saad ZS (2010) Defining functional SMA and pre-SMA subregions in human MFC using resting state fMRI: functional connectivity-based parcellation method. *Neuroimage* 49:2375–2386.
- Kringelbach ML (2005) The human orbitofrontal cortex: linking reward to hedonic experience. *Nat Rev Neurosci* 6:691–702.
- Kringelbach ML, Rolls ET (2004) The functional neuroanatomy of the human orbitofrontal cortex: evidence from neuroimaging and neuropsychology. *Prog Neurobiol* 72:341–372.
- Lynd-Balta E, Haber SN (1994) The organization of midbrain projections to the ventral striatum in the primate. *Neuroscience* 59:609–623.
- Mackey S, Petrides M (2010) Quantitative demonstration of comparable architectonic areas within the ventromedial and lateral orbital frontal cortex in the human and the macaque monkey brains. *Eur J Neurosci* 32:1940–1950.
- Margulies DS, Vincent JL, Kelly C, Lohmann G, Uddin LQ, Biswal BB, Villringer A, Castellanos FX, Milham MP, Petrides M (2009) Precuneus shares intrinsic functional architecture in humans and monkeys. *Proc Natl Acad Sci U S A* 106:20069–20074.
- Meila M (2007) Comparing clusterings—an information based distance. *J Multivar Anal* 98:873–895.
- Mesulam MM, Mufson EJ (1982a) Insula of the old world monkey. I. Architectonics in the insulo-orbito-temporal component of the paralimbic brain. *J Comp Neurol* 212:1–22.
- Mesulam MM, Mufson EJ (1982b) Insula of the old world monkey. III: Efferent cortical output and comments on function. *J Comp Neurol* 212:38–52.
- Morecraft RJ, Geula C, Mesulam MM (1992) Cytoarchitecture and neural afferents of orbitofrontal cortex in the brain of the monkey. *J Comp Neurol* 323:341–358.
- Morrison SE, Salzman CD (2009) The convergence of information about rewarding and aversive stimuli in single neurons. *J Neurosci* 29:11471–11483.
- Mufson EJ, Mesulam MM (1982) Insula of the old world monkey. II: Afferent cortical input and comments on the claustrum. *J Comp Neurol* 212:23–37.

- Murray EA, O'Doherty JP, Schoenbaum G (2007) What we know and do not know about the functions of the orbitofrontal cortex after 20 years of cross-species studies. *J Neurosci* 27:8166–8169.
- Nelson SM, Cohen AL, Power JD, Wig GS, Miezin FM, Wheeler ME, Velanova K, Donaldson DI, Phillips JS, Schlaggar BL, Petersen SE (2010) A parcellation scheme for human left lateral parietal cortex. *Neuron* 67:156–170.
- O'Doherty J, Kringelbach ML, Rolls ET, Hornak J, Andrews C (2001) Abstract reward and punishment representations in the human orbitofrontal cortex. *Nat Neurosci* 4:95–102.
- O'Doherty J, Dayan P, Schultz J, Deichmann R, Friston K, Dolan RJ (2004) Dissociable roles of ventral and dorsal striatum in instrumental conditioning. *Science* 304:452–454.
- Ongür D, Price JL (2000) The organization of networks within the orbital and medial prefrontal cortex of rats, monkeys and humans. *Cereb Cortex* 10:206–219.
- Ongür D, Ferry AT, Price JL (2003) Architectonic subdivision of the human orbital and medial prefrontal cortex. *J Comp Neurol* 460:425–449.
- Padoa-Schioppa C, Assad JA (2006) Neurons in the orbitofrontal cortex encode economic value. *Nature* 441:223–226.
- Park SQ, Kahnt T, Rieskamp J, Heekeren HR (2011) Neurobiology of value integration: when value impacts valuation. *J Neurosci* 31:9307–9314.
- Porrino LJ, Goldman-Rakic PS (1982) Brainstem innervation of prefrontal and anterior cingulate cortex in the rhesus monkey revealed by retrograde transport of HRP. *J Comp Neurol* 205:63–76.
- Sajonz B, Kahnt T, Margulies DS, Park SQ, Wittmann A, Stoy M, Ströhle A, Heinz A, Northoff G, Bermpohl F (2010) Delineating self-referential processing from episodic memory retrieval: common and dissociable networks. *Neuroimage* 50:1606–1617.
- Schultz W, Dayan P, Montague PR (1997) A neural substrate of prediction and reward. *Science* 275:1593–1599.
- Stevens WD, Buckner RL, Schacter DL (2010) Correlated low-frequency BOLD fluctuations in the resting human brain are modulated by recent experience in category-preferential visual regions. *Cereb Cortex* 20:1997–2006.
- Tomassini V, Jbabdi S, Klein JC, Behrens TE, Pozzilli C, Matthews PM, Rushworth MF, Johansen-Berg H (2007) Diffusion-weighted imaging tractography-based parcellation of the human lateral premotor cortex identifies dorsal and ventral subregions with anatomical and functional specializations. *J Neurosci* 27:10259–10269.
- Tremblay L, Schultz W (1999) Relative reward preference in primate orbitofrontal cortex. *Nature* 398:704–708.
- Uylings HB, Sanz-Arigita EJ, de Vos K, Pool CW, Evers P, Rajkowska G (2010) 3-D cytoarchitectonic parcellation of human orbitofrontal cortex correlation with postmortem MRI. *Psychiatry Res* 183:1–20.
- Van Dijk KR, Hedden T, Venkataraman A, Evans KC, Lazar SW, Buckner RL (2010) Intrinsic functional connectivity as a tool for human connectomics: theory, properties, and optimization. *J Neurophysiol* 103:297–321.
- Vincent JL, Patel GH, Fox MD, Snyder AZ, Baker JT, Van Essen DC, Zempel JM, Snyder LH, Corbetta M, Raichle ME (2007) Intrinsic functional architecture in the anaesthetized monkey brain. *Nature* 447:83–86.
- Wager TD, Lindquist MA, Nichols TE, Kober H, Van Snellenberg JX (2009) Evaluating the consistency and specificity of neuroimaging data using meta-analysis. *Neuroimage* 45:S210–S221.
- Walker AE (1940) A cytoarchitectural study of the prefrontal area of the macaque monkey. *J Comp Neurol* 73:59–86.
- Wallis JD (2007) Orbitofrontal cortex and its contribution to decision-making. *Annu Rev Neurosci* 30:31–56.
- Weiskopf N, Hutton C, Josephs O, Deichmann R (2006) Optimal EPI parameters for reduction of susceptibility-induced BOLD sensitivity losses: a whole-brain analysis at 3 T and 1.5 T. *Neuroimage* 33:493–504.
- Williams SM, Goldman-Rakic PS (1998) Widespread origin of the primate mesofrontal dopamine system. *Cereb Cortex* 8:321–345.
- Zald DH, Rauch S (2008) *The orbitofrontal cortex*. New York: Oxford UP.
- Zhang D, Snyder AZ, Fox MD, Sansbury MW, Shimony JS, Raichle ME (2008) Intrinsic functional relations between human cerebral cortex and thalamus. *J Neurophysiol* 100:1740–1748.